Working Doc SEM simulation

Duy Duc NGUYEN

December 2019

1 Introduction

Process control in microelectronics consists in measuring metrics experimentally and to compare these values to the targeted ones. If a too large deviation is observed, the ongoing process is reworked or, if not possible, the product is recycled. The most common technique used for dimensional metrology is top-view Scanning Electron Microscopy (SEM) due to its reasonable throughput and to its numerous automatic pattern detection and automatic dimension measurement toolbox. SEM consists in scanning the sample with a narrow focused electron beam that is accelerated at a given energy and to detect the electrons that are "emitted" by the sample during the scanning. SEM system is showed in Figure 1. By synchronizing the beam position with the detected signal, an image is recorded. Physics that occurs during the scanning of the sample involve interaction of electrons with matter, [5] diffusion of charges in excess, charge migration and recombination of the charges [15, 14]. Electrons matter interactions can be simulated using a Monte Carlo approach [2, 5, 16] or it can be approximated using a compact model that uses a Point Spread function [1]. Electron matter interactions are processes that can be considered as static while diffusion and recombination are dynamic. The purpose of this work is to model these dynamic processes using FEniCS, a solver that implements the Finite Element Method. Previously published paper pointed out that charge diffusion and migration is strongly depends of the material as expected [12]. In order to generate an artificial SEM image, emitted electrons must be taken into account. It was demonstrated that emission yield of electron from the sample is mathematically formulated by a Robin boundary condition at the specimen's surface [14, 15, 8]. Following these existing models, we are able to create artifact SEM images base on the amount of SEE which will be reported in this report. However, most of the models have not taken into account the transport of emitted electrons in the vacuum chamber which will positively come back to the specimen when there are local charging areas affecting their trajectory in addition to the electrical field created by the detector. We will report our technique to take into account this phenomenon.
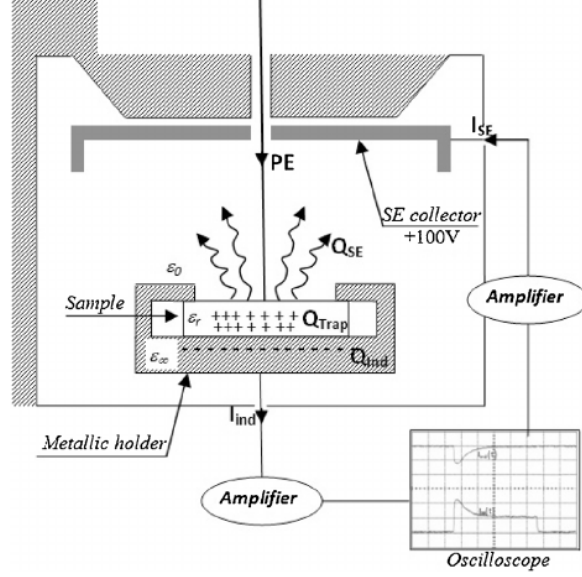
Figure 1: SEM system scheme [8].

2 Drift-diffusion model

2.1 With vacuum domain

The drift diffusion model computed in this study defines a system of three Partial Differential Equations (PDEs) that takes into account the dynamic variation of the electron density, hole density and the induced electrical field that appears when an excess of positive or negative charges exists or when an electron detector is in action. Electron and hole densities will tend to equilibrate with time but the SEM beam generates source terms that set the system in a non-equilibrium state. The transport equations for particle movements in semiconductor sample is given by

$$
\begin{cases}
\varepsilon \nabla \cdot \boldsymbol{E} = \dfrac{q_e}{\varepsilon_0}\left(p - n\right) & \text{in } \Omega_0 \times (0, t_{end}] \\
\dfrac{\partial n}{\partial t} + \nabla \cdot \boldsymbol{j}_n = S_n - R & \text{in } \Omega_0 \times (0, t_{end}] \\
\dfrac{\partial p}{\partial t} + \nabla \cdot \boldsymbol{j}_p = S_p - R & \text{in } \Omega_0 \times (0, t_{end}]
\end{cases}
\tag{1}
$$

where Ω_0 is semiconductor sample, $t \in (0, t_{end}]$ is time variable, p and n are hole and electron densities respectively, $\boldsymbol{E} = -\nabla\varphi$ is electric field and φ is potential, ε_0 is absolute permittivity of the vacuum and ε is relative permittivity, q_e is the elementary charge, $\boldsymbol{j}_n$ and $\boldsymbol{j}_p$ are density currents, S_n and S_p are sources of electron and hole and R is recombination function. The electrons are the only particles that will emit from the semiconductor's surface and also the only source of electrons in vacuum. So that, the transport equation for electron movement in vacuum is given by

$$
\begin{cases}
\varepsilon \nabla \cdot \boldsymbol{E} = \dfrac{q_e}{\varepsilon_0}\left(-n\right) & \text{in } \Omega_1 \times (0, t_{end}] \\
\dfrac{\partial n}{\partial t} + \nabla \cdot \boldsymbol{j}_n = 0 & \text{in } \Omega_1 \times (0, t_{end}]
\end{cases}
\tag{2}
$$

where Ω_1 is vacuum domain. For more detail, please see Figure 2. For the shake of simplicity, hereafter, the equations will be written with a subperscribe 0 or 1 regarding its domain. The particle density currents in the semiconductor sample are given by

$$j_n^0 = n^0 \left(-\mu_n^0 \boldsymbol{E}^0\right) - D_n^0 \nabla n^0 \text{ and } j_p^0 = p^0 \left(\mu_p^0 \boldsymbol{E}^0\right) - D_p^0 \nabla p^0 \tag{3}$$

where μ is the drift mobility and $D\left(\mu\right) = \mu kT/q_e$ is the diffusion coefficient computed by Einstein relation and $\boldsymbol{v}_d = \mu \boldsymbol{E}$ is the drift velocity which shows that the electrons move in the opposite direction while the holes move in the same direction of the electrical field. The particle density currents in the vacuum [11] is given by

$$j_n^1 = n^1 \left(-\mu_n^1 \boldsymbol{E}^1\right) \text{ where } \mu_n^1 = \sqrt{\frac{2q_e}{m_e}|\varphi|}\frac{1}{|\boldsymbol{E}|} \tag{4}$$

which indicates that the speed of electrons in vacuum is proportional to the magnitude of the potential (free acceleration); as the electrons come closer to the potential source (the detector in our case) the speed will be larger.
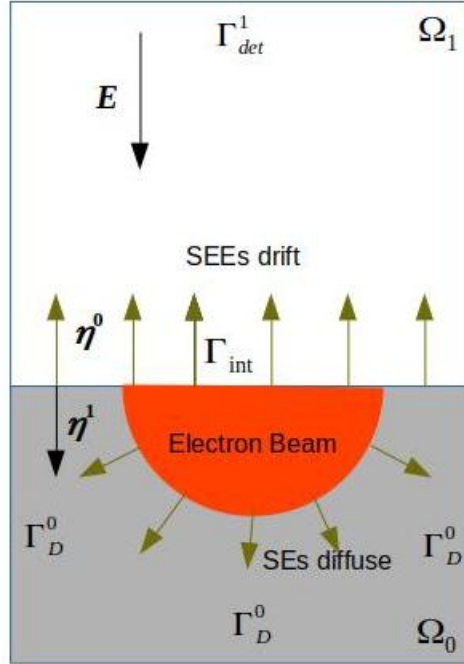

Figure 2: Semiconductor Ω_0 and vacuum Ω_1 scheme.

2.2 Sources and recombination

The electrons and holes source terms S_n and S_p are approximated thanks to Gauss functions. The holes source term S_p is assumed to be a small fraction of S_n

$$S_n = \frac{I_0}{q(2\pi)^{3/2}\sigma_x\sigma_y\sigma_z}exp\left(-\left(\frac{(x-Bx)^2}{\sigma_x^2} + \frac{(y-(By-0.3P))^2}{\sigma_y^2}\right)\right), S_p = 10^{-5}S_n \tag{5}$$

The electron beam scans the sample with time, Bx, By being the coordinate of the center of the spot. A shift in the z direction, denoted as P , is inputted. This shift corresponds to the maximum penetration depth of the electrons into the material [15, 14]. The order of magnitude of P is a few nanometers. The 2D Gauss function is defined with two spreading values σ_x, σ_y that correspond respectively to the width and the length of the electron interaction volume. This interaction volume is dependent of the material

but moreover it depends of the incident electron beam energy. For CD-SEM, electron energies are usually below $10[keV]$, the spreading ranges are then in the order of few tenth of nanometer. I_0 is the current of the electron beam, typical values ranging from tens of picoamperes up to nanoamperes. Once electrons are entrapped in the sample due to the incident beam, a rapid recombination appears that tends to compensate for this electron excess so electro-neutrality is maintained shortly. The recombination term, denoted by R, follows the Shockley-Read-Hall model formulated as

$$R\left(n^0, p^0\right) = \frac{n^0 p^0 - n_i^2}{\tau_p\left(n^0 + n_i\right) + \tau_n\left(p^0 + p_i\right)} \tag{6}$$

where n_i and p_i are the intrinsic carrier concentration, τ_n and τ_p the electron and hole average lifetimes.

2.3 Boundary conditions, initial conditions and computing SEE

Boundary conditions are used together with the governing equations to describe physical phenomena occurring at the boundaries. They also make the system can be solved and the solution is unique. The interface boundary condition mathematically shows how the variables exchange their values between two different domains. In general, the variables are not continuous at the interface. The Dirichlet boundary conditions shows that the variables will take exact values on it. And the Neumann boundary conditions shows the flux of the variables in or out a domain. The initial conditions show how each variable behaves in the beginning of simulation time $t = 0$.

Interface boundary condition: On Γ_{int}, the potential φ is assumed to be passes by a rate of $0 < \alpha_\varphi < 1$, so that the potentials created by the charges in the semiconductor sample or the potential created by the detector will have influences on each other. The transmission speed of φ can be neglected since it is solved in the favor of steady state. Similar to the electrons n, they pass the interface with a certain rate α_n and speed measured at the interface. However, the holes p are not allow to pass the interface since they are not exist in vacuum. These conditions are written as follow [8]

$$\begin{cases} \varepsilon^0 \nabla\varphi^0 \cdot \boldsymbol{\eta}^0 = -\varepsilon^1 \nabla\varphi^1 \cdot \boldsymbol{\eta}^1 = \alpha_\varphi\left(\varphi^1 - \varphi^0\right) & \text{on } \Gamma_{int} \\ \boldsymbol{j}_n^0 \cdot \boldsymbol{\eta}^0 = -\boldsymbol{j}_n^1 \cdot \boldsymbol{\eta}^1 = \alpha_n\left(\left|\boldsymbol{v}_{d,n}^0\right| n^0 - \left|\boldsymbol{v}_{d,n}^0\right| n^1\right) & \text{on } \Gamma_{int} \\ \boldsymbol{j}_p^0 \cdot \boldsymbol{\eta}^0 = -\boldsymbol{j}_p^1 \cdot \boldsymbol{\eta}^1 = 0 & \text{on } \Gamma_{int} \end{cases} \tag{7}$$

where $\boldsymbol{v}_d$ denotes the drift velocity of n, $\boldsymbol{\eta}$ denotes the normal outward vector, and α_n denote transmission coefficients satisfying $0 < \alpha_n < 1$ [3, 7]. These velocities are computed by [8]

$$\left|\boldsymbol{v}_{d,n}^0\right| = \sqrt{\frac{3k_B T}{m_e} + \left(\mu_n^0\left|\boldsymbol{E}^0\right|\right)^2} \text{ and } \left|\boldsymbol{v}_{d,n}^1\right| = \mu_n^1\left|\boldsymbol{E}^1\right| \tag{8}$$

where $|.|$ is norm of a vector, for instant, $|\boldsymbol{E}| = |-\nabla\varphi| = \sqrt{\nabla\varphi \cdot \nabla\varphi} = \sqrt{\sum_{i=1}^3\left(\frac{\partial\varphi}{\partial x_i}\right)^2}$, k_B denotes Boltzmann constant, T denotes temperature, m_e denotes mass of electron.

Dirichlet boundary conditions: On Γ_D, the electrons and holes will take the initial values since we assumed that far from the beam source, charges will be not increasing or the semiconductor sample is in contact with metal (Ohmic contact). The potential created by the charges there are too small, so that it will be considered as 0. The detector is placed above the sample surface about 2 cm and it has 100 V imposed. In our simulation, the vacuum domain is about 100 nm above the sample surface, so that the potential is scaled to 10^{-3} V to maintain the electrical field. The boundary conditions are written as follow

$$\begin{cases} n^0 = n_i, p^0 = p_i, \varphi^0 = 0 & \text{on } \Gamma_D \\ \varphi^1 = 10^{-3} & \text{on } \Gamma_{det} \end{cases}. \tag{9}$$

Neumann boundary condition: To avoid the escaping electrons accumulate too much in the vacuum domain without diffusion, they are allowed to go through Γ_{det} freely. In other words, a flux-out boundary

condition is applied on Γ_{det} as written below

$$\boldsymbol{j}_n^1 \cdot \boldsymbol{\eta}^1 = \left| \boldsymbol{v}_{d,n}^1 \right| n^1 \text{ on } \Gamma_{det}. \tag{10}$$

Initial conditions: At $t = 0$, the amount of electrons and holes in the sample are as natural; i.e intrinsic carrier concentration $n^0 = n_i$, $p^0 = p_i$ and $n^1 = p^1 = 0$, while the potential is formed by the detector which has been turned on before the scanning process. Thus, $\varphi(t = 0)$ is the solution of the following model

$$\begin{cases} \varepsilon \nabla \cdot \boldsymbol{E} = 0 & \text{in } \Omega \\ \varphi = 10^{-3} & \text{on } \Gamma_{det}^1 \\ \varepsilon^0 \nabla \varphi^0 \cdot \boldsymbol{\eta}^0 = -\varepsilon^1 \nabla \varphi^1 \cdot \boldsymbol{\eta}^1 = \alpha_\varphi \left(\varphi^1 - \varphi^0 \right) & \text{on } \Gamma_{int} \end{cases} \tag{11}$$

SEE computation: The detector, synchronized with the current position of the beam, collects the secondary electron emission from all over the top surface and during the irradiation time at one spot t_{spot}. This is represented by the following equation

$$SEE = \int_{t_{spot}} \int_{\Gamma_{det}} \boldsymbol{j}_n^1 \cdot \boldsymbol{\eta}^1 \, \mathrm{d}s \mathrm{d}t. \tag{12}$$

2.4   Without vacuum domain

In case of the vacuum domain is remove, only the system of PDEs in Ω_0 is kept and the interface boundary condition is simplified into the Robin boundary condition

$$\boldsymbol{j}_n \cdot \boldsymbol{\eta} = \alpha_n \left(n - n_i \right) \text{ on } \Gamma_{int}. \tag{13}$$

3   Weak forms

FEM is a numerical method for solving PDEs systems. The typical implementation consists in transforming the PDE system in a single integral formula named the weak form, that must be minimized during the simulation. The transformation of the PDE system into this weak form is obtained by multiplying each equation of the PDEs with test functions $\overline{\varphi}, \overline{n}, \overline{p}$ that are taken arbitrarily from an appropriate functional space containing functions that vanish on Γ_D and Γ_{det}; then integrate them over the related domain and apply Green's first identity at the term which has the highest order in derivative. Precisely, $\int_\Omega \nabla \cdot \nabla u v \, \mathrm{d}x = -\int_\Omega \nabla u \cdot \nabla v \, \mathrm{d}x + \int_{\partial \Omega} \nabla u \cdot \boldsymbol{\eta} v \, \mathrm{d}s$ where $\partial \Omega$ denotes the boundaries of Ω. For short, we will denote the integration over a domain and a boundary by $(u, v) = \int_\Omega uv \, \mathrm{d}x, \langle u, v \rangle_\Gamma = \int_\Gamma uv \, \mathrm{d}s$. The weak form is defined as the sum of all of these expressions and denoted by F.

3.1   With vacuum domain

The first step of the process of getting F is given as follow from (1) and (2) give us

$$\varepsilon^0 \left(\nabla \varphi^0, \nabla \overline{\varphi}^0 \right) - \frac{q_e}{\varepsilon_0} \left(p^0 - n^0, \overline{\varphi}^0 \right) - \left\langle \varepsilon^0 \nabla \varphi^0 \cdot \boldsymbol{\eta}^0, \overline{\varphi}^0 \right\rangle_{int} = 0,$$

$$\left(\frac{\partial n^0}{\partial t}, \overline{n}^0 \right) - \left(\boldsymbol{j}_n^0, \nabla \overline{n}^0 \right) - \left(S_n^0 - R^0, \overline{n}^0 \right) + \left\langle \boldsymbol{j}_n^0 \cdot \boldsymbol{\eta}^0, \overline{n}^0 \right\rangle_{int} = 0,$$

$$\left(\frac{\partial p^0}{\partial t}, \overline{p}^0 \right) - \left(\boldsymbol{j}_p^0, \nabla \overline{p}^0 \right) - \left(S_p^0 - R^0, \overline{p}^0 \right) + \left\langle \boldsymbol{j}_p^0 \cdot \boldsymbol{\eta}^0, \overline{p}^0 \right\rangle_{int} = 0, \tag{14}$$

$$\varepsilon^1 \left(\nabla \varphi^1, \nabla \overline{\varphi}^1 \right) - \frac{q_e}{\varepsilon_0} \left(-n^1, \overline{\varphi}^1 \right) - \left\langle \varepsilon^1 \nabla \varphi^1 \cdot \boldsymbol{\eta}^1, \overline{\varphi}^1 \right\rangle_{int} = 0,$$

$$\left(\frac{\partial n^1}{\partial t}, \overline{n}^1 \right) - \left(\boldsymbol{j}_n^1, \nabla \overline{n}^1 \right) + \left\langle \boldsymbol{j}_n^1 \cdot \boldsymbol{\eta}^1, \overline{n}^1 \right\rangle_{det} + \left\langle \boldsymbol{j}_n^1 \cdot \boldsymbol{\eta}^1, \overline{n}^1 \right\rangle_{int} = 0.$$

5

Before computing the boundary integrals, we introduce two useful notations; jump of a function $[\![a]\!] = a_0 - a_1$ and average of a function $\{a\} = 0.5\,(a_0 + a_1)$. One can check this consequency $[\![ab]\!] = \{a\}\,[\![b]\!] + [\![a]\!]\,\{b\}$. Applied these notations to a general infterface condition $c^0 \nabla u^0 \cdot \boldsymbol{\eta}^0 = -c^1 \nabla u^1 \cdot \boldsymbol{\eta}^1 = \alpha\,(u^1 - u^0)$, we get $[\![c\nabla u \cdot \boldsymbol{\eta}^0]\!] = 0$ and $\{c\nabla u \cdot \boldsymbol{\eta}^0\} = \alpha\,(u^1 - u^0) = -\alpha\,[\![u]\!]$. Therefore, $\langle \nabla u^0 \cdot \boldsymbol{\eta}^0, \overline{u}^0 \rangle + \langle \nabla u^1 \cdot \boldsymbol{\eta}^1, \overline{u}^1 \rangle = \langle \nabla u^0 \cdot \boldsymbol{\eta}^0, \overline{u}^0 \rangle - \langle \nabla u^1 \cdot \boldsymbol{\eta}^0, \overline{u}^1 \rangle = [\![\langle \nabla u \cdot \boldsymbol{\eta}^0, \overline{u} \rangle]\!] = \int_\Gamma [\![\nabla u \cdot \boldsymbol{\eta}^0 \overline{u}]\!] \ \mathrm{d}s = \int_\Gamma \{\nabla u \cdot \boldsymbol{\eta}^0\}\,[\![\overline{u}]\!] + [\![\nabla u \cdot \boldsymbol{\eta}^0]\!]\,\{\overline{u}\} \ \mathrm{d}s = -\alpha\,\langle [\![u]\!], [\![\overline{u}]\!] \rangle$. Applying these results to (7) we get, $[\![\varepsilon \nabla \varphi \cdot \boldsymbol{\eta}^0]\!] = 0, \{\varepsilon \nabla \varphi \cdot \boldsymbol{\eta}^0\} = -\alpha_\varphi\,[\![\varphi]\!]$ and $[\![\boldsymbol{j}_n \cdot \boldsymbol{\eta}^0]\!] = 0, \{\boldsymbol{j}_n \cdot \boldsymbol{\eta}^0\} = \alpha_n\,[\![|\boldsymbol{v}_n|\,n]\!]$ so that

$$\langle \varepsilon^0 \nabla \varphi^0 \cdot \boldsymbol{\eta}^0, \overline{\varphi}^0 \rangle_{int} + \langle \varepsilon^1 \nabla \varphi^1 \cdot \boldsymbol{\eta}^1, \overline{\varphi}^1 \rangle_{int} = -\,\alpha_\varphi\,\langle [\![\varphi]\!], [\![\overline{\varphi}]\!] \rangle_{int}, \tag{15}$$
$$\langle \boldsymbol{j}_n^0 \cdot \boldsymbol{\eta}^0, \overline{n}^0 \rangle_{int} + \langle \boldsymbol{j}_n^1 \cdot \boldsymbol{\eta}^1, \overline{n}^1 \rangle_{int} = \alpha_n\,\langle [\![|\boldsymbol{v}_n|\,n]\!], [\![\overline{n}]\!] \rangle_{int}.$$

Summing all equations in (14) and applying (15) (10) to the result, we get the final F

$$F_\varphi = \varepsilon^0\,\left(\nabla \varphi^0, \nabla \overline{\varphi}^0\right) + \varepsilon^1\,\left(\nabla \varphi^1, \nabla \overline{\varphi}^1\right) - \frac{q_e}{\varepsilon_0}\,\left(p^0 - n^0, \overline{\varphi}^0\right) - \frac{q_e}{\varepsilon_0}\,\left(-n^1, \overline{\varphi}^1\right) + \alpha_\varphi\,\langle [\![\varphi]\!], [\![\overline{\varphi}]\!] \rangle_{int},$$

$$F_n = \left(\frac{\partial n^0}{\partial t}, \overline{n}^0\right) + \left(\frac{\partial n^1}{\partial t}, \overline{n}^1\right) - \left(\boldsymbol{j}_n^0, \nabla \overline{n}^0\right) - \left(S_n^0 - R^0, \overline{n}^0\right) - \left(\boldsymbol{j}_n^1, \nabla \overline{n}^1\right) + \alpha_n\,\langle [\![|\boldsymbol{v}_n|\,n]\!], [\![\overline{n}]\!] \rangle_{int} + \langle |\boldsymbol{v}_{d,n}^1|\,n^1, \overline{n}^1 \rangle_{det},$$

$$F_p = \left(\frac{\partial p^0}{\partial t}, \overline{p}^0\right) - \left(\boldsymbol{j}_p^0, \nabla \overline{p}^0\right) - \left(S_p^0 - R^0, \overline{p}^0\right),$$

$$F = F_\varphi + F_n + F_p. \tag{16}$$

3.2   Without vacuum domain

Follow the same procedure but without the system (2), we get the model

$$F_\varphi = \varepsilon\,(\nabla \varphi, \nabla \overline{\varphi}) - \frac{q_e}{\varepsilon_0}\,(p - n, \overline{\varphi})$$

$$F_n = \left(\frac{\partial n}{\partial t}, \overline{n}\right) - (\boldsymbol{j}_n, \nabla \overline{n}) + \langle \boldsymbol{j}_n, \overline{n} \rangle_{\Gamma_{int}} - (S_n - R, \overline{n})$$

$$F_p = \left(\frac{\partial p}{\partial t}, \overline{p}\right) - (\boldsymbol{j}_p, \nabla \overline{p}) - (S_p - R, \overline{p})$$

$$F = F_\varphi + F_n + F_p \tag{17}$$

4   Implementation in FEniCS

The general implementations such as the weak form and the Dirichlet boundary conditions are well discussed in [9]. Here we only discuss the implementation of the interface boundary condition. To do that, we can use either Partition of Unity Finite Element Method (PUFEM) [10] or Discontinuous Galerkin method. In this work, we use PUFEM since it is easier for maintaining, and for parallel computing. Because we have two sub-domains Ω_0 and Ω_1, we consider the variables φ, n and p as vector functions. Precisely, $(\varphi, n, p) \in H^2_{\Gamma_D \cup \Gamma_{det}}(\Omega) \times H^2_{\Gamma_D \cup \Gamma_{det}}(\Omega) \times H^2_{\Gamma_D \cup \Gamma_{det}}(\Omega)$ and $\varphi = \left(\varphi^0, \varphi^1\right)$, $n = \left(n^0, n^1\right)$ and $p = \left(p^0, p^1\right)$. From now, we will use u to represent φ, n, p. In general words, we only look at how u^0 and u^1 act on the sub-domains Ω^0 and Ω^1 respectively, despite that both of them are defined on the total domain Ω. The interface boundary condition acts as a bridge to connect them. This gives us two main problems during and after the solving process, namely stabilization and visualization.

Interface stabilization: Since only a half of u^0 or u^1 are used in the weak form, we need to add the other half but with a very small coefficient $\beta = 0.001$ to avoid its affection on the results. Precisely, each F_u will be added an additional term of $\beta \left(\int_{\Omega_0} u^1 \overline{u}^1 \ \mathrm{d}x + \int_{\Omega_1} u^0 \overline{u}^0 \ \mathrm{d}x \right)$, i.e.

$$F_u = F_u + \beta \left\{ \left(u^1, \overline{u}^1\right)_{\Omega^0} + \left(u^0, \overline{u}^0\right)_{\Omega^1} \right\}. \tag{18}$$

Visualization: After receiving the results, we need to "plot" $u^0|_{\Omega^0}$ and $u^1|_{\Omega^1}$ on the same domain Ω. Thus, they are projected to a Discontinuous Galerkin space of degree 0 to get the combined function u^r, i.e. u^r satisfies

$$\int_\Omega u^r \overline{u}^r \, \mathrm{d}x = \int_{\Omega_0} u^0 \overline{u}^r \, \mathrm{d}x + \int_{\Omega_1} u^1 \overline{u}^r \, \mathrm{d}x \text{ for all test function } \overline{u}^r. \tag{19}$$

Streamline stabilization: Furthermore, the drift-diffusion equation is actually a simpler version convection-diffusion-reaction equation which classically need to be stabilized. In this work, we use Galerkin Least Squares (GLS) technique [4], where the weak form F (16) will be added by

$$gls_u^i (u, \overline{u}) = \int_{\Omega_i} L_u^i (\overline{u}) \, \tau_u^i Res_u^i (u) \, \mathrm{d}x$$

where Res_u^i are strong residuals of (1) and L_u^i is divergence of the current densities; i.e.

$$L_u^i \left(u^i\right) = \nabla \cdot \boldsymbol{j}_u^i = \nabla \cdot \left(u^i \left(-\mu_u^i \boldsymbol{E}^i\right) - D\left(\mu_u^i\right)\right) \tag{20}$$

$$Res_n^i \left(n^i\right) = \frac{\partial n^i}{\partial t} + L_n^i \left(n^i\right) - S_n + R\left(n^i, p^i\right)$$

$$Res_p^0 \left(p^0\right) = \frac{\partial p^0}{\partial t} + L_p^0 \left(p^0\right) - S_p + R\left(n^0, p^0\right)$$

and τ_u^i is stabilization parameter [6] given by

$$\tau_u^i = \left(\frac{2}{h} + \frac{4\nu}{h^2}\right)^{-1} = \frac{h}{2\left|\boldsymbol{v}_{d,u}^i\right|} \left(1 + \frac{1}{Pe}\right)^{-1} ; Pe = \frac{\left|\boldsymbol{v}_d^i\right| h}{2D_u^i} \tag{21}$$

where Pe is Péclet number and h is a function which gives size of each mesh cell. In practice, h is scaled by a constant s_h, i.e. $h = s_h h$ and in our work s_h should be in $(0.1, 1)$. The weak forms are rewritten as follow

$$F_u = F_u + gls_u^i (u, \overline{u}) \tag{22}$$

Time scheme: We use backward Euler as our discretization scheme such as

$$\frac{\partial u}{\partial t} (t_{i+1}) = \frac{u(t_{i+1}) - u(t_i)}{dt} \tag{23}$$

where $t_i = idt \in (0, t_{end}]$, dt is time step defined by $dt = t_{end}/|i|$.

Adaptive mesh: Once the geometry is set and the materials chosen, a mesh must be generated to solve the system by the Finite Element Method. Using a uniform mesh with a small size would result in two many voxels therefore tremendously long computation time. Consequently, designing an adaptive mesh is mandatory. The designed adaptive mesh in this study is dense in the vicinity of the scanning area and in the electron spreading volume but is relaxed outside of the scanning area Figure 3.

Mixed solvers: In order to save time and resources, we prefer to use Newton-GMRES solver as a primitive solver which is lunched at each time step and followed by a Newton solver as a backup solver.

Adaptive time step: We use the simplest adaptive time step refinement which is based on the number of iterations. Precisely, dt will be doubled if the simulation at each time step converges less than 5 iterations otherwise it will be reduced by half. Our initial dt is $1E-5 ns$ as there is a lot of movement of electrons in vacuum at the beginning.
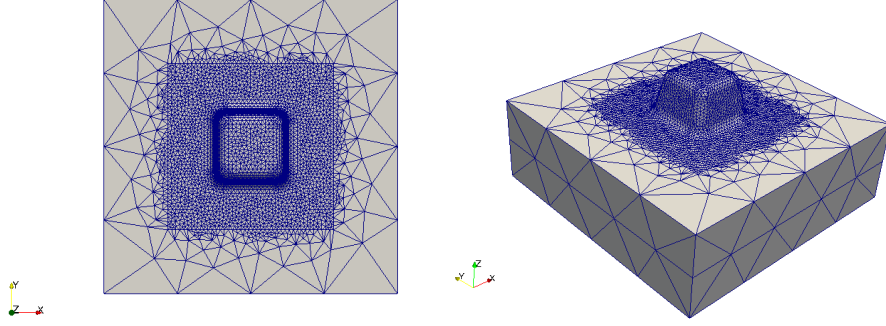
Figure 3: Adaptive mesh built on a 3D specimen, dense mesh is applied to the scanning area and coast mesh is applied to the remain area.

Parallel computation: In addition to the meshing technique, the parallel computing technique decomposes the mesh into many pieces according to the number of the used cores. For example, Figure 4 shows the mesh is decomposed into three pieces. In practice, 15 cores are used on a workstation at LTM laboratory and it reduces the computational time from 8 hours (with 1 core) to 1 hours.
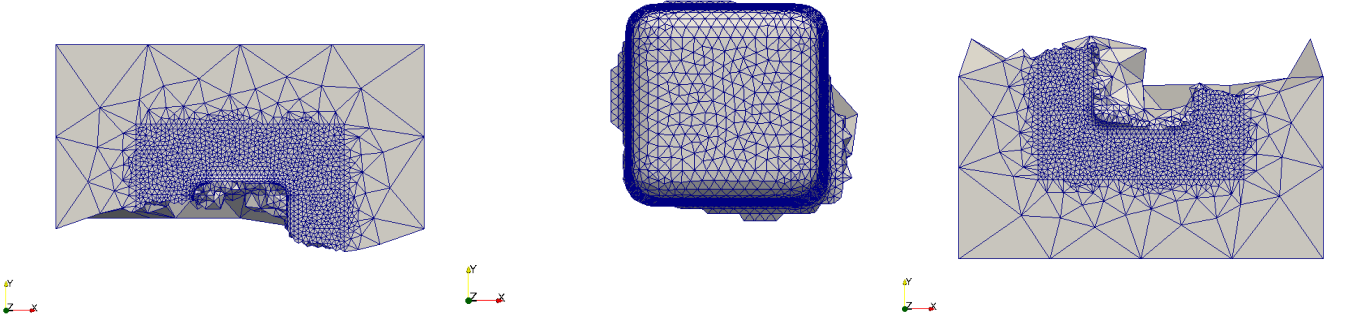
Figure 4: Mesh decomposition for parallel computing. In this case, three cores are used.

5   Numerical results

5.1   Simulation without vacuum

This work was presented at SPIE-AL 2019 in San Jose, CA, US [13]. In this work, the total domain is a rectangular substrate of $300 \times 300 \times 100 nm^3$ of size. On the top of the substrate, a trapezoid pattern is defined. Its size is set by $60 \times 60 \times 50 nm^3$, and a slope of 80^0. Two different materials will be considered, Silicon (Si) that is a semiconductor (fast charge diffusion and migration coefficient) and Silicon Dioxide (SiO2) which is a dielectric where charge diffusion and migration are slow. Once the geometry is set and the materials chosen, a mesh must be generated to solve the system by the Finite Element Method. Using a uniform mesh with a small size would result in two many voxels (3D pixels) therefore tremendously long computation time. The scanning area is $50[nm]$ larger than the pattern dimension and is centered at the pattern position. The beam step size during the scanning is set at $10[nm]$. On purpose, the scanning area is set smaller than the total domain size in order to avoid simulation errors close to the domain boundaries. The incident beam S_n fully scans the specimen starting from the left to the right and from the top to the bottom. It is defined to stay $5[\mu s]$ at each spot . The parameters in the source $\sigma_x = \sigma_y = \sigma_z$ whose dimensions are considered to be proportional with the material density. For Si it is set equal to $10[nm]$ and

to 8.7[nm] for SiO2. In order to minimize the residue for every time, it was chosen to use a backward Euler scheme for each time step 5[μs].
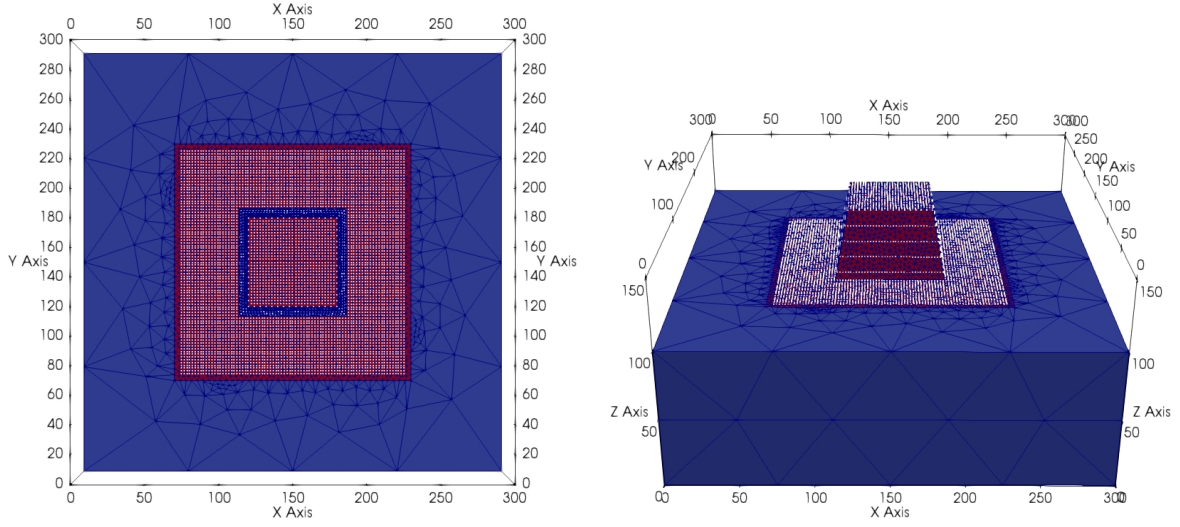

Figure 5: Plot of all beam spots (white dots) (Bx, By, Bz). The surface in red is scanning area where dense mesh is set, the remain surface in blue in blue is set with coast mesh. Only the scanning area will be shown in SEM image.

Figure 6 shows how electron density is spreading in the Silicon for three spot positions. At the very beginning (Figure 6(a)), electron density is high only in the vicinity of the spot due to the fast diffusion and migration of the charges in Silicon. When the spot is located at the center of the pattern (Figure 6(b)), electrons are slightly entrapped in the pattern due to the pattern boundaries that act as a diffusion and migration barrier. Finally, at the very end of the scan (Figure 6(c)), a similar electron spreading than for the initial beam position is observed. This proves that the rapid diffusion and migration of the charges prevent any charging effect due to the previously scanned surface. We can observe here that the FEM modeling is consistent with what is expected when considering the charging of semiconductor materials.
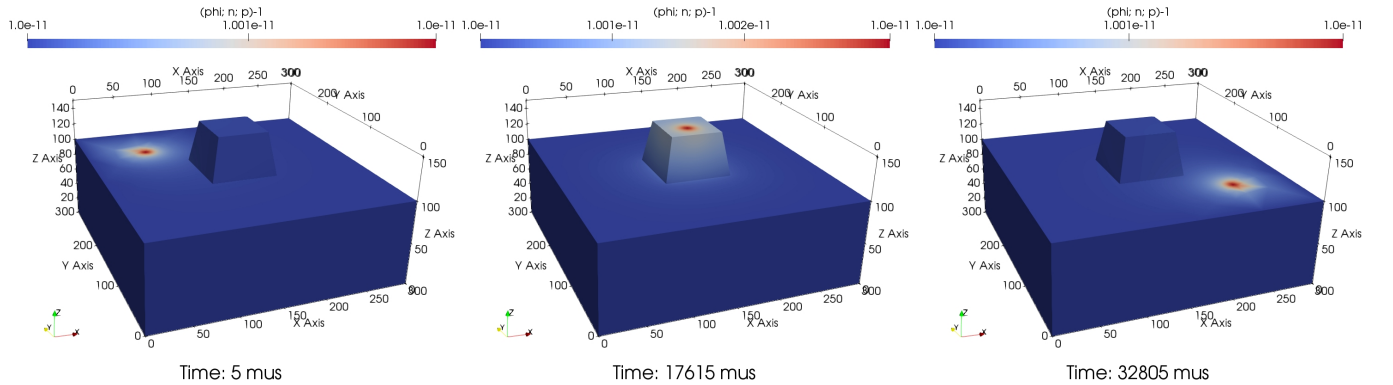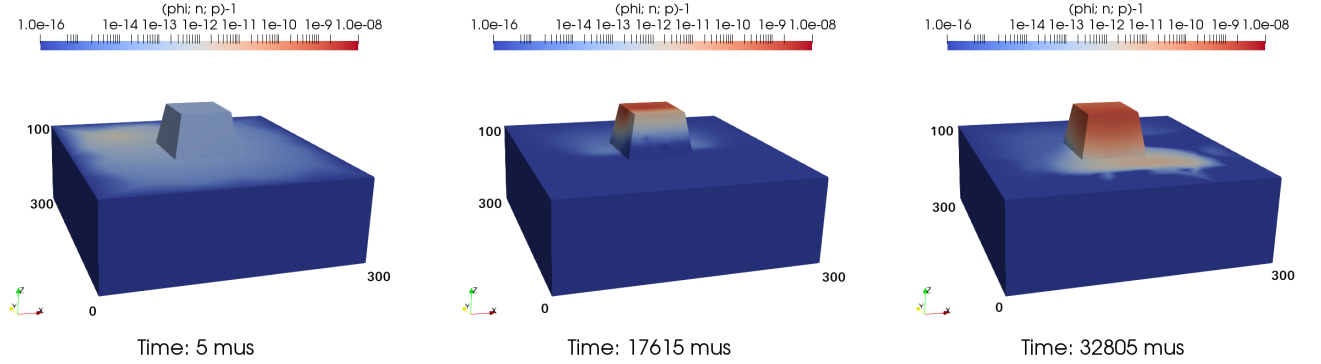

Figure 6: The concentration of electron in Si-Si Simulation at the beginning, at the middle and at the end of the scanning process.

Figure 7 shows the spreading of the electron densities in the SiO2 for the same spot positions as in

previous section. SiO2 is a dielectric so electron drift and diffusion are very slow compared to Si. Comparing Figure 7(a) with Figure 7(c), the electron density distribution does not look alike. This points out the charging of the sample during the scan. At the end of the scan, the pattern still shines with a high electron density in it. When the spot is located at the center of the pattern for the intermediate time (Figure 7(b)), electrons are entrapped in the pattern and an asymmetry is clearly observed. The previously scanned areas of the pattern still have a large electron density. These FEM results are consistent with the fact that charging effects more likely occur when scanning a dielectric sample with a SEM. Figure 7 focuses on the potential at the surface of the SiO2 sample at same three spot positions. It confirms the charging effect of the sample during the scanning. Obviously, it should be taken into account in the future in order to mitigate the SEE efficiency with its value.

Figure 7: The concentration of electron in SiO2-SiO2 Simulation at the beginning, at the middle and at the end of the scanning process.

The electrons escaping through Γ_{int} are taken into account in equation 12. The synthetic SEM image shown in Figure 9 obtained with SiO2 shows an anomalous contrast in the upper part compared to the lower part. We did expect that the total SEE at the later spot might be higher than the previous one due to the way of the detector collects electrons. The SEM detector response is modelled by integrating the SEE signal on the whole sample surface during the time the spot stays at a given position. Because of the previously scanned surface, the detector collects electrons that escape the sample surface due to the spot by itself but it also collects electrons that escapes from other previously scanned area where charges are still in excess. SEE emission only stops when the electron concentration reaches the intrinsic electron density, i.e $n = n_i$. As for Si patterns, the concentration of electron increases as expected when the pattern is scanned. Again, the pattern boundaries act as a diffusion and migration barrier so less freedom is allowed to charges to move. Those electrons will slowly diffuse and therefore will continue to contribute to the SEE signal until the end of the scanning process. The SEE signal generated by the pattern is a main contributor for the detector. Looking at the contrast of the the artifact SEM signal in the middle of the pattern, it looks quite similar to the real contrast obtained when a real SEM measures CD of patterns. But the anomalous contrast in the vertical direction points out an imperfect calibration of the model, certainly due to the detector modelling or to the surface potential that impacts on SEE efficiency.
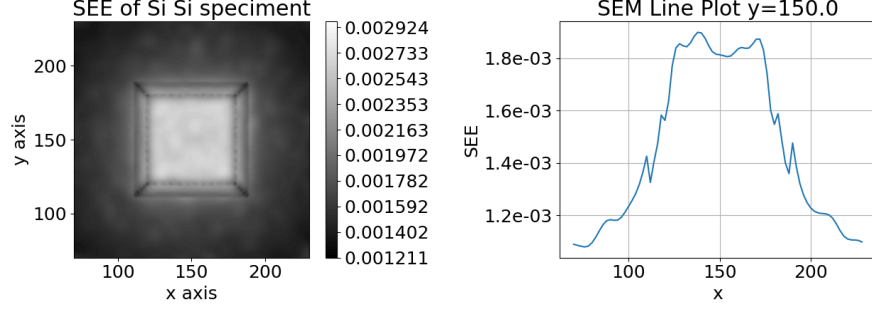
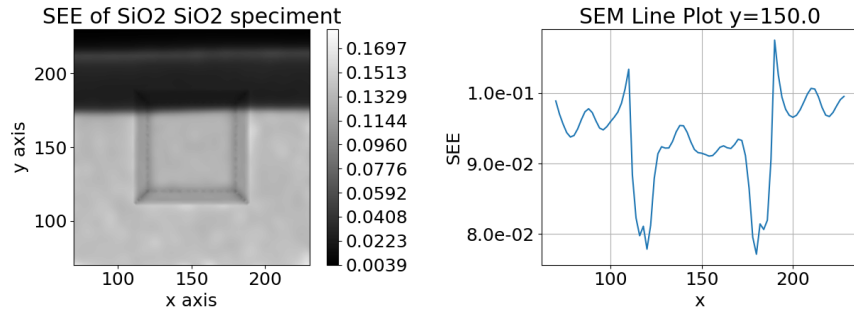Figure 8: Synthetic SEM image of Si-Si simulation and SEM signal measurement at $y = 150[nm]$.

Figure 9: Synthetic SEM image of SiO2 -SiO2 simulation and SEM signal measurement at $y = 150[nm]$.

5.2 Simulation with vacuum

Due to the time limitation, we only have 2D simulations at the moment of witting this report. In this work, a cross section of a substrate of $900 \times 150nm^2$ is simulated. On the top of the substrate, three trapezoid pattern are placed. Their sizes are set by $50 \times 150nm^2$, and a slope of 80^0, Figure 10. The incident beam S_n scans all the patterns starting from the left to the right. The beam step size during the scanning is set at $2[nm]$. It is defined to stay $50[ns]$ at each spot. The parameters in the source $\sigma_x = \sigma_y = 10[nm]$ whose dimensions are considered to be proportional with the material density. And each spot takes a depth of $By = P := 0.7\sigma_x$ from the surface where P is called electron maximum penetration, Figure 11. The transmission coefficients α_n and α_φ are assumed to be 0.8 both.
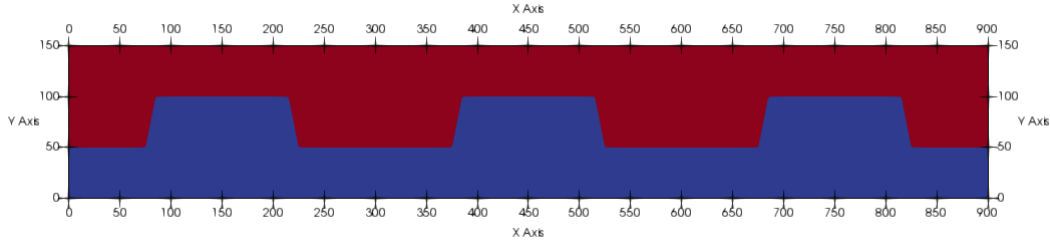

Figure 10: 2D domain with a specimen marked in blue and a vacuum marked in red. The substrate has a size of $900 \times 150nm^2$ and three patterns of size $150 \times 50nm^2$.
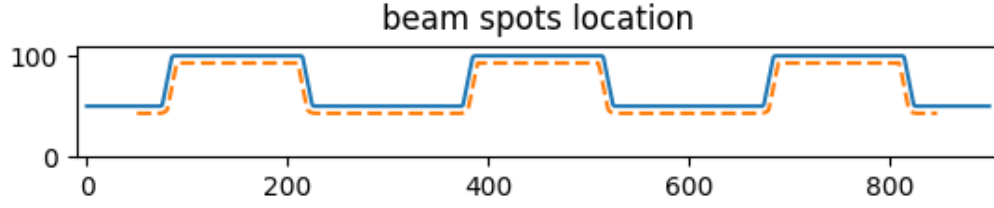
11

Figure 11: Plot of all beam spots (Bx, By), By are kept a distance of P to the surface.

In the beginning, only intrinsic carrier concentrations n_i and p_i contain in the substrate while the electric field is set up in the vacuum and the substrate by the detector, Figure 12.
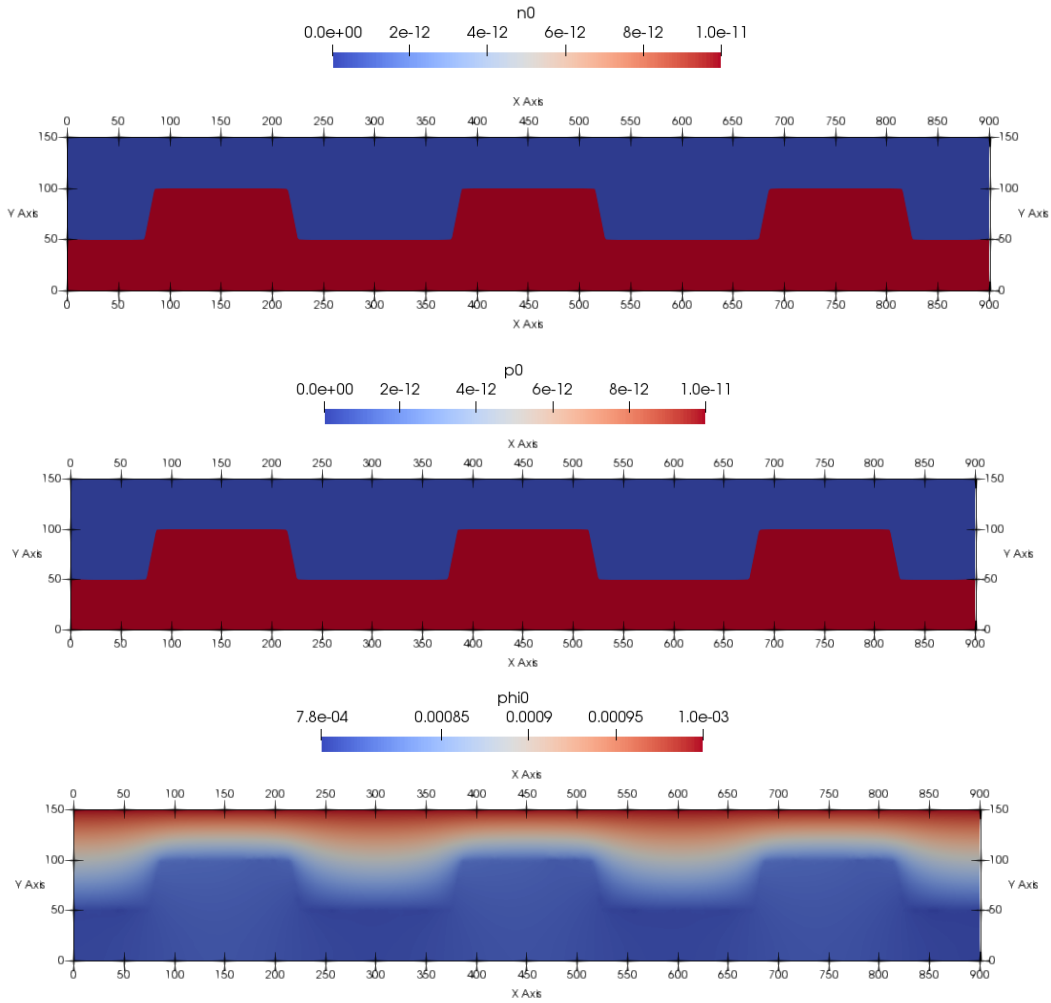

Figure 12: Initial set up of n, p and φ

Figure 13 shows how electron density is spreading in the Si and the vacuum for three spot positions. At the beginning, the very first secondary electrons drift from the specimen surface into the vacuum chamber.

When the spot is located at the center of the second pattern, more secondary electrons escape into vacuum chamber due to the pattern boundaries that act as a diffusion and migration barrier. Finally, at the end of the scan, secondary electrons continue to escape from the current spot and also form the previous spots.
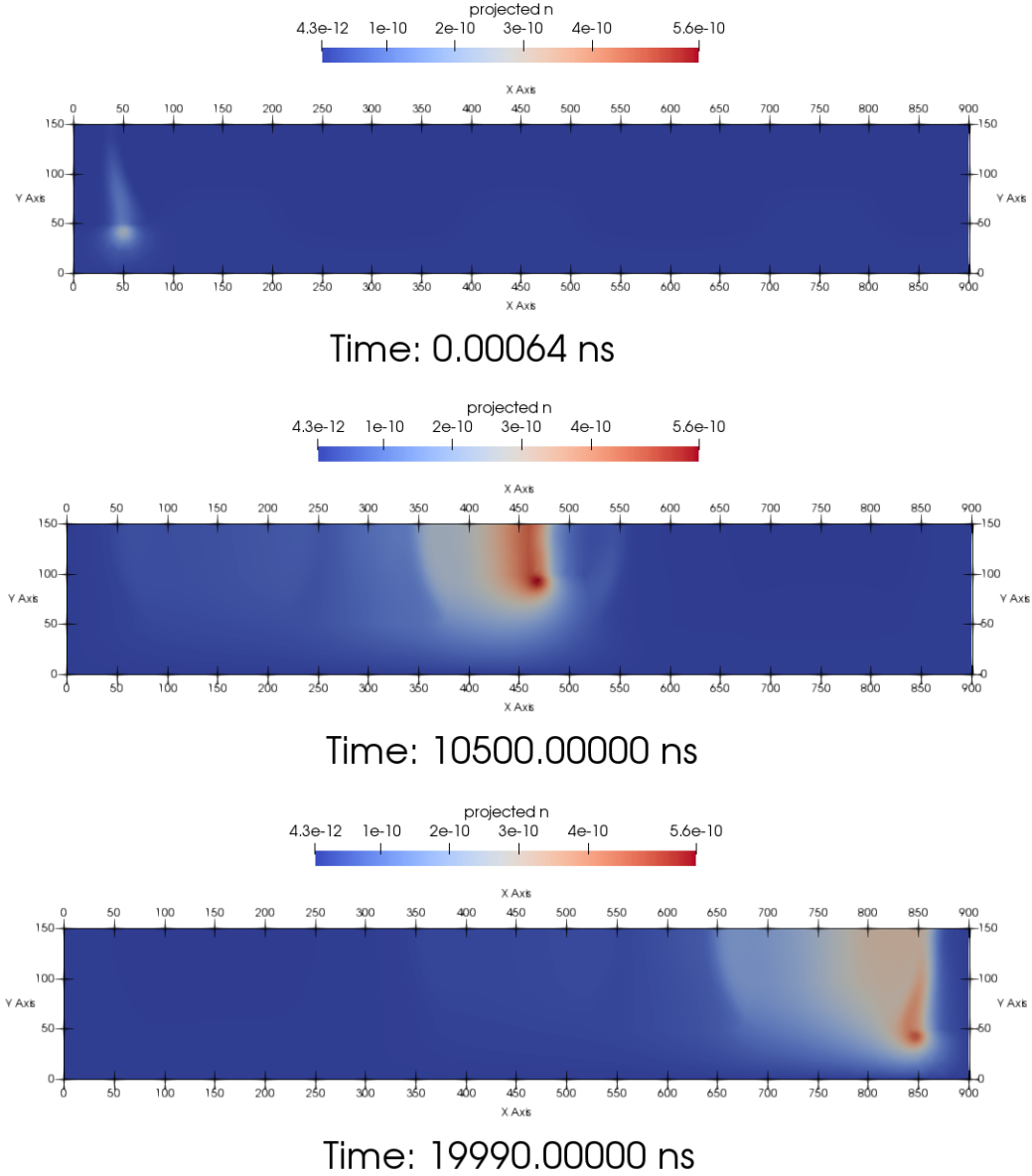

Time: 0.00064 ns

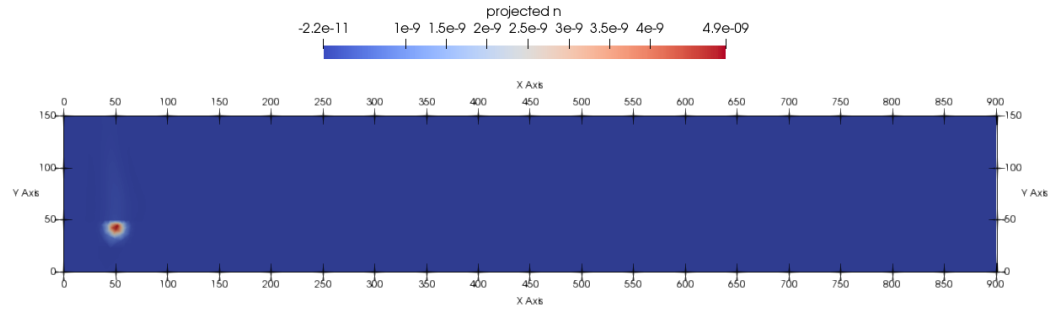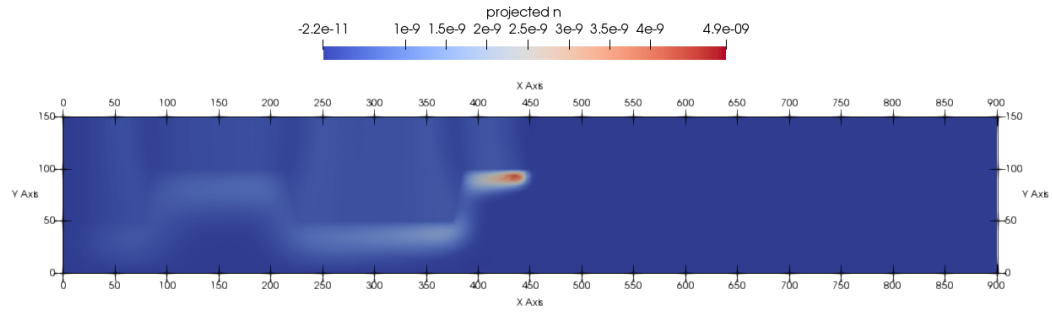Time: 10500.00000 ns

Time: 19990.00000 ns

Figure 13: The concentration of electron in the Si substrate and the vacuum at the beginning, at the middle and at the end of the scanning process.

Figure 14 shows how electron density is spreading in the SiO2 and the vacuum for three spot positions. The process is similar to the case of Si except the concentration of electron in the substrate at each spot is higher and the amount of secondary electrons escaping from the specimen is smaller. This phenomenon is caused by the diffusion and drift coefficients of SiO2 are smaller than ones in Si.

13

Time: 20.97153 ns

Time: 9840.00000 ns
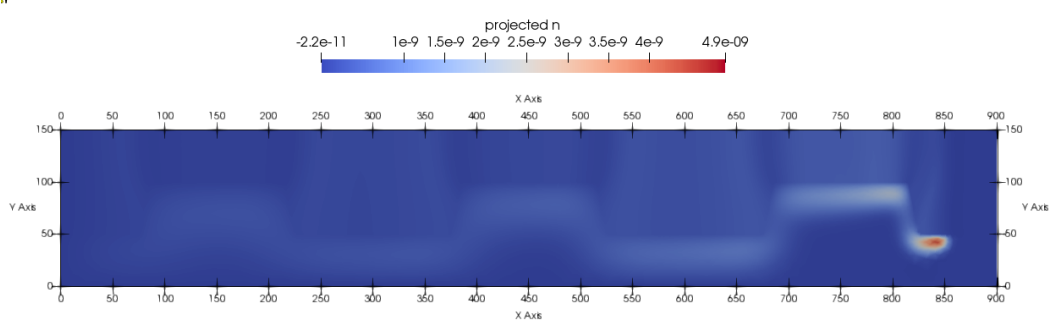
Time: 19990.00000 ns

Figure 14: The concentration of electron in the SiO2 substrate and the vacuum at the beginning, at the middle and at the end of the scanning process.

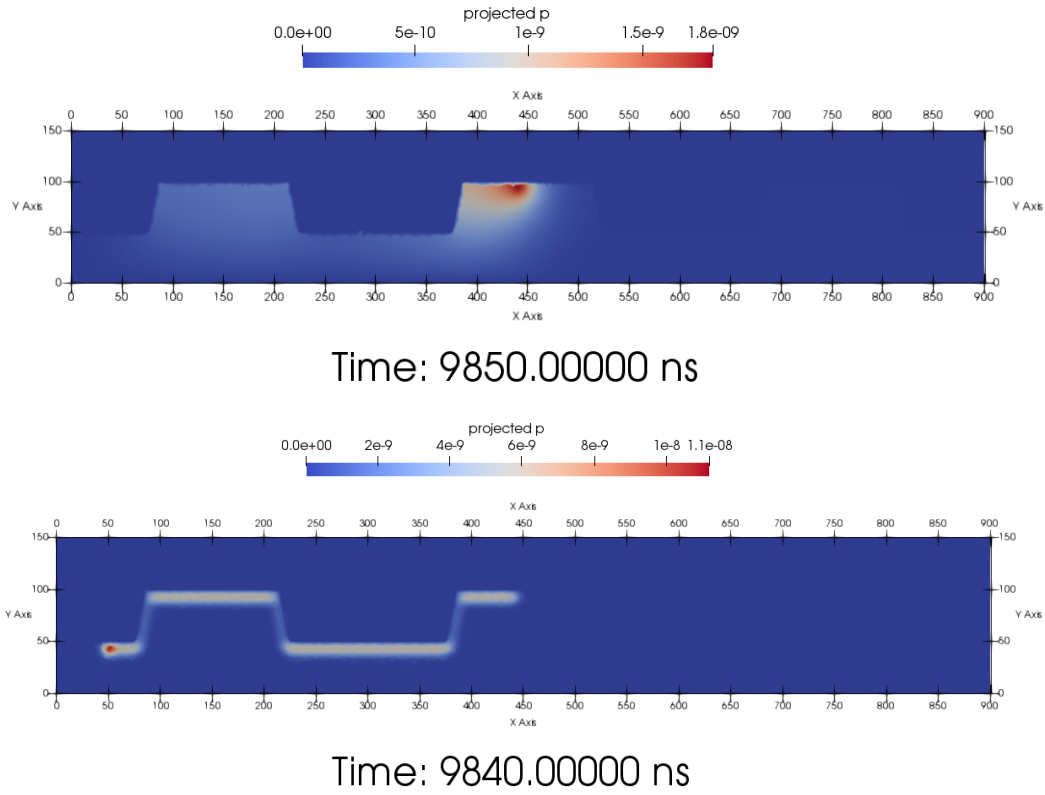Figure 15 shows the concentrations of hole during the scanning process of Si and SiO2 specimens.

Time: 9850.00000 ns

Time: 9840.00000 ns

Figure 15: The concentration of hole in the substrate during the scanning process of Si (upper) and SiO2 (lower).

Figure 16 shows the electric filed forms in the specimen and vacuum during the scanning process of Si and SiO2. In the vacuum, the electric field shows the direction for secondary electrons to flow.
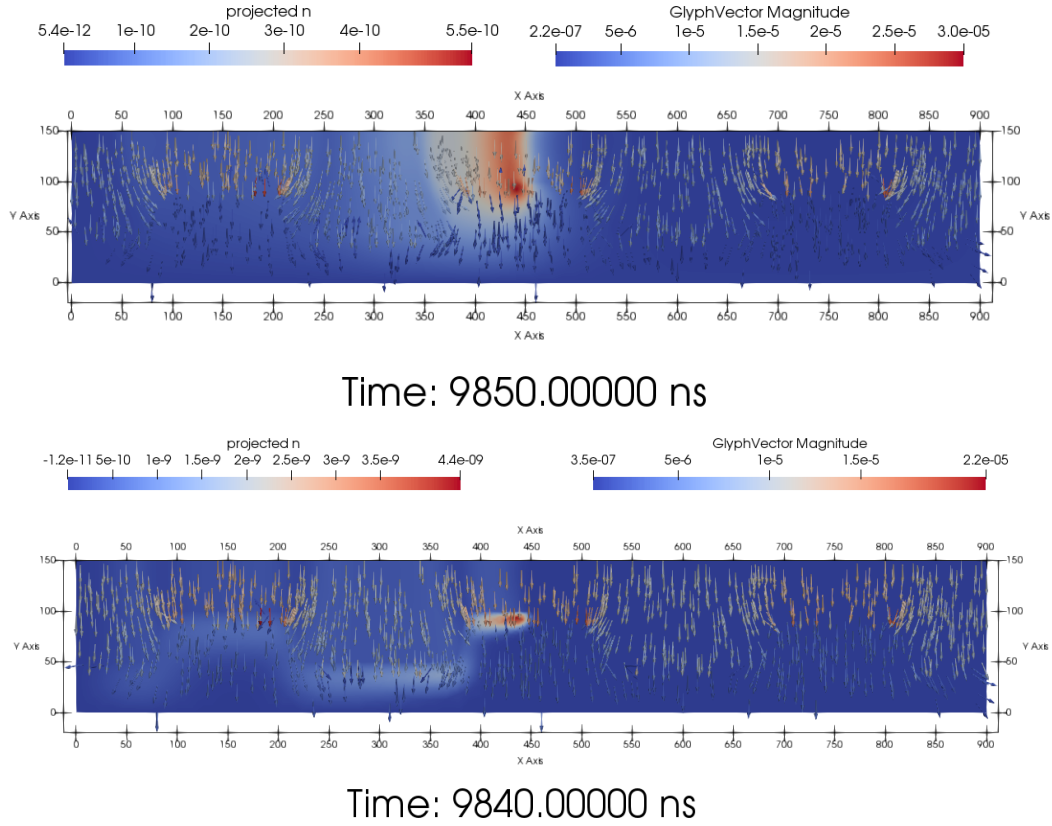
Time: 9850.00000 ns

Time: 9840.00000 ns

Figure 16: Electric field forms in the substrate and vacuum during the scanning process of Si (upper) and SiO2 (lower).

Figure 17 shows the amount of secondary electrons flow through the top boundary of the vacuum domain at each spot, during the irritation time t_{spot} versus the spots of Si and SiO2 simulations. Assume that these electrons are totally collected by the detector, then they are the SEM signals.
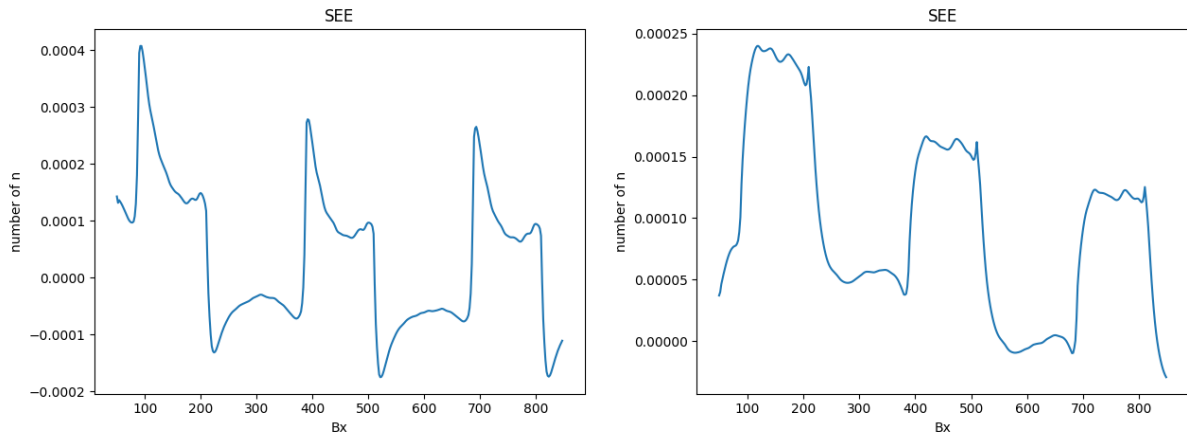

Figure 17: SEM signals of 2D simulation of Si (left) and SiO2 (right)

Repeating the SEM signals shown in Figure 17 to a xy-plane of spots, we are able to generate artifact SEM images that are shown in Figure 18.
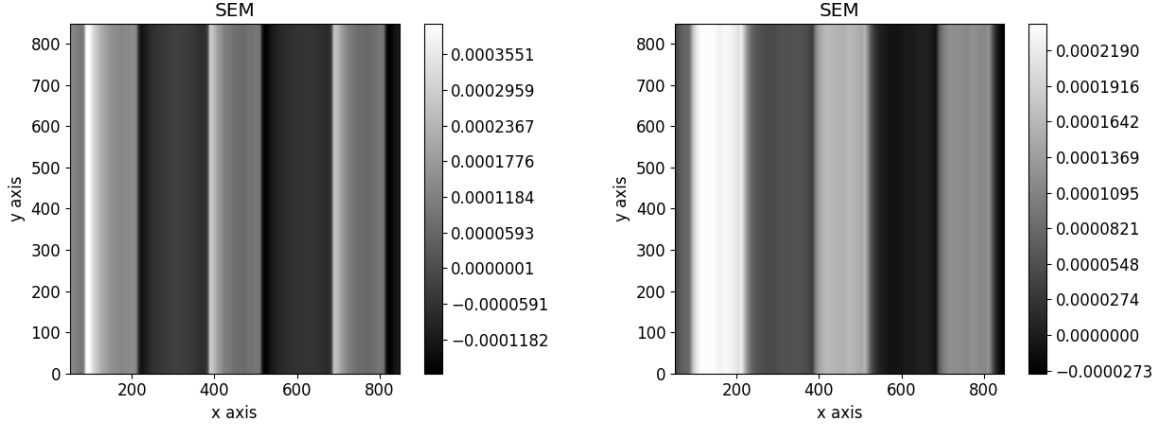

Figure 18: SEM images created from 2D simulations of Si (left) and SiO2 (right)

6   Conclusion and future works

The vacuum domain really plays an important role for the result. We observer the edge effects and the charging effects in Figure 17, 18. In the case of Si sample, the left edge is brighter than the right edge and the first pattern is brighter than the rest. Similar to the case of SiO2, but the signal is so noisy.

In the future, we can implement a better adaptive time refinement such as Richardson Extrapolation, a better adaptive mesh refinement such as Goal Oriented Adaptive Mesh Refinement. The SEM signal should be calibrated with Monte Carlo simulation software such as Casino, JMONSEL or Chariot Figure 19.
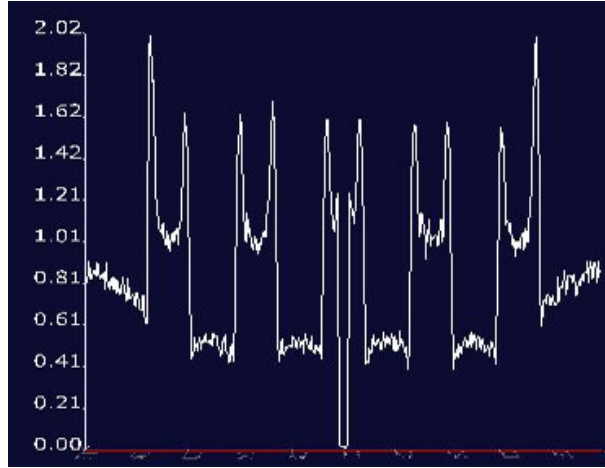

Figure 19: Chariot SEM signal

FEM is promising to solve this problem since it is able to handle many physics happening at the same time. The next interesting phenomena is heat transfer and heat expansion. When the heat model is successfully implement and calibrated, it can be merge with the drift-diffusion model.

Notation	Unit	Value (Si, SiO2)	Refs
k_B	CV/K	1.38E-23	
T	K	300	
m_e	$CVns^2/nm^2$	0.911E-30	
q_e	C	1.6E-19	
μ_n	nm^2/Vns	1400.0E5, 20.0E5	
μ_p	nm^2/Vns	500.0E5, 4.0E-4	
D_n	nm^2/ns		
ε	1	11.68, 3.9	
ε_0	C/Vnm	8.854E-21	
n_i	nm^{-3}	1E-16	
p_i	nm^{-3}	1E-16	
τ_n	ns	1E4	
τ_p	ns	1E4	
t	ns		
t_{spot}	ns	1E3	

Table 1: Table of parameters

Appendix

Parameters

Change unit of all parameters

c is speed of light in vacuum $c = 2.99792458 \times 10^8 m/s$

$[nm] = 10^{-9} [m] ; [ns] = 10^{-9} [s] ; \left[\frac{J}{c^2}\right] = \frac{1}{c_0^2}\left[\frac{CV}{\left(\frac{m}{s}\right)^2}\right] = \frac{1}{c_0^2}\left[\frac{CVs^2}{m^2}\right] = \frac{10^{18}}{c_0^2 10^{18}}\left[\frac{CVns^2}{nm^2}\right] = \frac{1}{c_0^2}\left[\frac{CVns^2}{nm^2}\right] ;$

$m_e = 8.1871057769 \times 10^{-14} \left[\frac{J}{c^2}\right] = \frac{8.1871057769 \times 10^{-14}}{(2.99792458\times 10^8)^2}\left[\frac{CVns^2}{nm^2}\right] = 0.9109383701584688 \times 10^{-30} \left[\frac{CVns^2}{nm^2}\right]$

Check unit

First, we compute the unit of small terms

(5) $S_n = \frac{I0}{q_e(2\pi)^{3/2}\sigma_x\sigma_y\sigma_z}exp\left(-\left(\frac{(x-Bx)^2}{\sigma_x^2} + \frac{(y-By)^2}{\sigma_y^2} + \frac{(z-Bz)^2}{\sigma_z^2}\right)\right)$ so that $[S_n] = \frac{C/ns}{Cnm^3} = \frac{1}{nm^3ns}$

(6) $R\left(n^0, p^0\right) = \frac{n^0p^0 - n_i^2}{\tau_p(n^0+n_i)+\tau_n(p^0+p_i)}$ so that $[R] = \frac{\frac{1}{nm^3}\frac{1}{nm^3} - \frac{1}{nm^3}\frac{1}{nm^3}}{ns\left(\frac{1}{nm^3}+\frac{1}{nm^3}\right)+ns\left(\frac{1}{nm^3}+\frac{1}{nm^3}\right)} = \frac{\frac{1}{nm^6}}{ns\frac{1}{nm^3}} = \frac{1}{nm^3ns}$

(4b) $\mu_n^1 = \sqrt{\frac{q_e}{m_e}|\varphi|}\frac{1}{|\boldsymbol{E}|}$ so that $[\mu_n^1] = \sqrt{\frac{C}{\frac{CVns^2}{nm^2}}V}\frac{1}{\sqrt{\frac{V^2}{nm^2}}} = \sqrt{\frac{Cnm^2}{CVns^2}V}\frac{nm}{V} = \frac{nm^2}{nsV}$

(4a) (8b) $\boldsymbol{v}_{d,n}^1 = -\mu_n^1\boldsymbol{E}^1$ so that $\left[\boldsymbol{v}_{d,n}^1\right] = \frac{nm^2}{nsV}\frac{V}{nm} = \frac{nm}{ns}$

(8a) $\left|\boldsymbol{v}_{d,n}^0\right| = \sqrt{\frac{3k_BT}{m_e} + \left(\mu_n^0\left|\boldsymbol{E}^0\right|\right)^2}$ so that $\left[\left|\boldsymbol{v}_{d,n}^0\right|\right] = \sqrt{\frac{\frac{CV}{K}K}{\frac{CVns^2}{nm^2}} + \left(\frac{nm^2}{Vns}\frac{V}{nm}\right)^2} = \frac{nm}{ns}$

We check the balance of the unit in the equations (1) (2). The summary can be found in the Table 2

(3) $\boldsymbol{j}_n^0 = n^0\left(-\mu_n^0\boldsymbol{E}^0\right) - D_n^0\nabla n^0$ so that $[\boldsymbol{j}_n^0] = \frac{1}{nm^3}\left(\frac{nm^2}{Vns}\frac{V}{nm}\right) + \frac{nm^2}{ns}\frac{1}{nm^4} = \frac{1}{nm^2ns}$

(3) $\boldsymbol{j}_p^0 = p^0\left(\mu_p^0\boldsymbol{E}^0\right) - D_p^0\nabla p^0$ so that $[\boldsymbol{j}_p^0] = \frac{1}{nm^2ns}$

(4a) $\boldsymbol{j}_n^1 = n^1\left(-\mu_n^1\boldsymbol{E}^1\right)$ so that $[\boldsymbol{j}_n^1] = \frac{1}{nm^3}\frac{nm}{ns} = \frac{1}{nm^2ns}$

(1a) $\varepsilon\nabla \cdot \boldsymbol{E} = \frac{q_e}{\varepsilon_0}\left(p - n\right)$ so that $[lhs] = 1\frac{V}{nm^2}$, $[rhs] = \frac{C}{C/Vnm}\frac{1}{nm^3} = \frac{V}{nm^2}$

(1b) $\frac{\partial n}{\partial t} + \nabla \cdot \boldsymbol{j}_n = S_n - R$ so that $[lhs] = \frac{1}{nm^3ns} + \frac{1}{nm}\frac{1}{nm^2ns} = \frac{1}{nm^3ns}$, $[rhs] = \frac{1}{nm^3ns} - \frac{1}{nm^3ns} = \frac{1}{nm^3ns}$

(1c) $\frac{\partial p}{\partial t} + \nabla \cdot \boldsymbol{j}_p = S_p - R$ so that $[lhs] = \frac{1}{nm^3 ns} + \frac{1}{nm}\frac{1}{nm^2 ns} = \frac{1}{nm^3 ns}$, $[rhs] = \frac{1}{nm^3 ns}$

(2a) and (2b) are similar.

Boundary conditions:

on Γ_{det}

(9)

on the interface

(15a)$\varepsilon^0 \nabla \varphi^0 \cdot \boldsymbol{\eta}^0 = -\varepsilon^1 \nabla \varphi^1 \cdot \boldsymbol{\eta}^1 = \alpha_\varphi \left(\varphi^1 - \varphi^0 \right)$ so that $[lhs] = 1\frac{V}{nm}nm = V$, $[rhs] = 1V$

(15b) $\boldsymbol{j}^0 \cdot \boldsymbol{\eta}^0 = -\boldsymbol{j}^1 \cdot \boldsymbol{\eta}^1 = \alpha_n \left(\left| \boldsymbol{v}_{d,n}^0 \right| n^0 - \left| \boldsymbol{v}_{d,n}^0 \right| n^1 \right)$ so that $[lhs] = \frac{1}{nm^2 ns}nm = \frac{1}{nmns}$, $[rhs] = \frac{nm}{ns}\frac{1}{nm^2} = \frac{1}{nmns}$ not that n is compute on $2D$ boundary

$\left| v_{d,n}^0 \right| = \sqrt{\frac{3k_B T}{m_e} + \left(\mu_n^0 \left| \boldsymbol{E}^0 \right| \right)^2}$

$\left[\!\left[\left| v_{d,n}^0 \right| \right]\!\right] =$

(10)

(12) $SEE = \int_{t_{spot}} \int_{\Gamma_{det}} \boldsymbol{j}_n^1 \cdot \boldsymbol{\eta}^1 \, \mathrm{d}s\mathrm{d}t$ so that $[SSE] =$

In general, it is defined by the multiplication of the charge density and the velocity

Notation	Unit	Notation	Unit
n	$1/nm^3$		
p	$1/nm^3$		
φ	V		
$\boldsymbol{E}$	V/nm		
$\boldsymbol{j}_n$	$1/nm^2 ns$		
$\boldsymbol{j}_p$	$1/nm^2 ns$		
S_n			
S_p	nm^2/ns		
R			

Table 2: Table of variables

References

[1] Benjamin Alles, Eric Cotte, Bernd Simeon, and Timo Wandel. Modeling the work piece charging during e-beam lithography. In *SPIE Advanced Lithography*, pages 69244P–69244P. International Society for Optics and Photonics, 2008.

[2] Sergey Babin, Sergey S Borisov, Hiroyuki Ito, Andrei Ivanchikov, and Makoto Suzuki. Simulation of scanning electron microscope images taking into account local and global electromagnetic fields. *Journal of Vacuum Science & Technology B, Nanotechnology and Microelectronics: Materials, Processing, Measurement, and Phenomena*, 28(6):C6C41–C6C47, 2010.

[3] Jacques Cazaux. About the charge compensation of insulating samples in xps. *Journal of Electron Spectroscopy and Related Phenomena*, 113(1):15–33, 2000.

[4] Ramon Codina. Comparison of some finite element methods for solving the diffusion-convection-reaction equation. *Computer Methods in Applied Mechanics and Engineering*, 156(1-4):185–210, 1998.

[5] Dominique Drouin, Alexandre Réal Couture, Dany Joly, Xavier Tastet, Vincent Aimez, and Raynald Gauvin. Casino v2. 42 a fast and easy-to-use modeling tool for scanning electron microscopy and microanalysis users. *Scanning*, 29(3):92–101, 2007.

[6] Joel H Ferziger and Milovan Perić. *Computational methods for fluid dynamics*, volume 3. Springer, 2002.

[7] HJ Fitting, H Glaefeke, and W Wild. Attenuation length and escape depth of excited electrons in solids. *Surface Science*, 75(2):267–278, 1978.

[8] N Ghorbel, A Kallel, and G Damamme. Analytical model of secondary electron emission yield in electron beam irradiated insulators. *Micron*, 112:35–41, 2018.

[9] Hans Petter Langtangen and Anders Logg. *Solving PDEs in Python*. Springer, 2017.

[10] Jens M Melenk and Ivo Babuška. The partition of unity finite element method: basic theory and applications. *Computer methods in applied mechanics and engineering*, 139(1-4):289–314, 1996.

[11] Robert David Middlebrook. A modern approach to semiconductor and vacuum device theory. *Proceedings of the IEE-Part B: Electronic and Communication Engineering*, 106(17S):887–902, 1959.

[12] Duy Duc Nguyen, Jean-Herve Tortai, Mohamed Abaidi, and Patrick Schiavone. Fem simulation of charging effect during sem metrology. In *34th European Mask and Lithography Conference*, volume 10775, page 107750P. International Society for Optics and Photonics, 2018.

[13] Duy Duc Nguyen, Jean-Herve Tortai, and Patrick Schiavone. Fem simulation for artificial generation of sem pictures. In *Metrology, Inspection, and Process Control for Microlithography XXXIII*, volume 10959, page 1095918. International Society for Optics and Photonics, 2019.

[14] Behrouz Raftari, Neil Budko, and Kees Vuik. A modified and calibrated drift-diffusion-reaction model for time-domain analysis of charging phenomena in electron-beam irradiated insulators. *AIP Advances*, 8(1):015307, 2018.

[15] Behrouz Raftari, NV Budko, and C Vuik. Self-consistent drift-diffusion-reaction model for the electron beam interaction with dielectric samples. *Journal of Applied Physics*, 118(20):204101, 2015.

[16] John S Villarrubia, AE Vladár, Bin Ming, Regis J Kline, Daniel F Sunday, JS Chawla, and Scott List. Scanning electron microscope measurement of width and shape of 10nm patterned lines using a jmonsel-modeled library. *Ultramicroscopy*, 154:15–28, 2015.